Chemical Science

ROYAL SOCIETY OF CHEMISTRY

EDGE ARTICLE

View Article Online
View Journal | View Issue

Check for updates

Cite this: *Chem. Sci.*, 2026, **17**, 4978

All publication charges for this article have been paid for by the Royal Society of Chemistry

Highly stable linking of platinum and porous spinel *via* carbon bridge engineering towards a long-lifespan rechargeable zinc–air battery

Mei Wang, *[a] Hao Du,[a] Yong Nian,[a] Guanshui Ma, [b] Jinfang Zhang,[a] Xiaoguang Wang *[c] and Xiaofeng Li *[a]

Received 19th December 2025
Accepted 12th January 2026

DOI: 10.1039/d5sc09967f

rsc.li/chemical-science

The development of bifunctional oxygen electrocatalysts is crucial for the commercialization of rechargeable zinc–air batteries (RZABs). This work proposes an innovative strategy of "dealloying–carbon coating–dip pyrolysis" for the highly stable anchoring of a small amount of Pt nanoparticles (0.032 mg cm^{-2}) onto carbon-encapsulated nanoporous $CoFe_2O_4$ (np-CFO). Benefiting from its nanoporous structure with a larger specific surface area and adhered carbon layer with superior electrical conductivity, the sandwich-like Pt/np-CFO@C electrode exhibits a lower OER–ORR potential gap (ΔE) of 0.7 V. Meanwhile, a Pt/np-CFO@C-based RZAB delivers a specific capacity of 781 mA h g^{-1}, power density of 185 mW cm^{-2} and cycling life exceeding 1400 hours. FTIR and XAFS results indicate that the carbon layer could not only play a bridging role between np-CFO and Pt, but also lead to the loading of more zero-valent Pt. HAADF imaging proves that the post-formed oxide layer can protect Pt from inactivation through strong metal–support interaction (SMSI). *In situ* Raman and RRDE testing confirm the 4-electron transfer mechanism of the ORR on Pt/np-CFO@C. DFT calculations verify that Pt/CFO@C has metallic properties, symmetric d-band centers and the lowest energy barrier for the ORR/OER. *In situ* XRD reveals that the size of Pt nanoparticles could become smaller in the early stage of discharge, which is beneficial for exposing more active sites and showing gradually improving performance. This study lays the groundwork for the future development of cost-effective RZABs.

Open Access Article. Published on 12 January 2026. Downloaded on 5/6/2026 12:28:05 AM.
This article is licensed under a Creative Commons Attribution-NonCommercial 3.0 Unported Licence.

Introduction

Driven by the global transition to clean and low-carbon energy, there is a critical need to develop advanced technologies for storing and converting energy efficiently and sustainably. The rechargeable zinc–air battery (RZAB) has been considered a promising candidate for future energy systems, originating from its high theoretical energy density (1086 Wh kg^{-1}), low cost, inherent safety, and environmental friendliness.[1,2] Nevertheless, the performance of RZAB is constrained primarily by the air cathode, where the oxygen evolution reaction (OER) and oxygen reduction reaction (ORR) occur during charging and discharging, respectively. Both these multi-step reactions involve complex four-electron transfer processes and suffer from sluggish reaction kinetics.[3,4] Although noble-metal catalysts (*e.g.*, RuO_2/IrO_2 for OER and Pt/C for ORR) demonstrate high activity in accelerating these reactions, their widespread application in RZABs is impeded by intrinsic limitations, including their high cost, low utilization, insufficient stability and monofunctional nature.[5,6] Consequently, the development of low-Pt-loaded, efficient and durable bifunctional oxygen electrocatalysts is crucial to lowering the energy barrier and enhancing the reversibility of RZABs.

In recent years, transition metal oxides (TMOs) have emerged as promising candidates to replace noble-metal-based catalysts for OER and ORR, which is attributable to their special 3d electronic orbits, superior stability and low cost.[7] As reported by Kumar and Fu,[8] Mn_3O_4 possesses multiple valence states and exceptional stability, as well as NiAl-LDH being made up of layered metal hydroxides with positive charges inserted between anions. Combining the advantages of both, the Mn_3O_4@NiAl-LDH heterostructure exhibits efficient electron hopping, a large specific surface area and abundant active sites, yielding a power density of 74.4 mW cm^{-2} and stable operation for over 300 h at 2 mA cm^{-2} when integrated into a ZAB. Li *et al.*[9] modified a $PrBaCo_2O_{6-\delta}$ electrode *via* Fe-doping and oxygen vacancy engineering, which could induce the partial conversion of perovskite into CoFeOOH, thus changing the OER pathway. Profiting from the intrinsic ORR activity of perovskite and the

[a]*School of Materials Science and Engineering, North University of China, Taiyuan 030051, China*

[b]*State Key Laboratory of Advanced Marine Materials, Zhejiang Key Laboratory of Extreme Environmental Material Surfaces and Interfaces, Ningbo Institute of Materials Technology and Engineering, Chinese Academy of Sciences, Ningbo 315201, China*

[c]*Laboratory of Advanced Materials and Energy Electrochemistry, School of Materials Science and Engineering, Taiyuan University of Technology, Taiyuan 030024, China*

© 2026 The Author(s). Published by the Royal Society of Chemistry

Open Access Article. Published on 12 January 2026. Downloaded on 5/6/2026 12:28:05 AM. This article is licensed under a Creative Commons Attribution-NonCommercial 3.0 Unported Licence.

OER activity of CoFeOOH, PBC-Q700 delivered a lower bifunctional potential differential of 117 mV. Even so, poor conductivity and layer/particle accumulation will still limit the efficiency of electronic transmission and the exposure of active sites.[10]

To improve these issues with TMOs, Peng *et al.*[11] found that an N-donor ligand in the carbon support could enhance the crystallinity of Fe_xO, accelerating electron transfer and increasing the conductivity of a V–Fe_xO/NC electrode. The corresponding ZAB possessed a more stable open circuit potential (1.46 V) and a higher specific capacity (743.0 mA h g^{-1}). Moreover, N-doped carbon could also cause electron spin polarization, reduce the band gap and optimize the adsorption/desorption property of Sc_2O_3.[12] In contrast, a TMO such as $FeCoO_x$ could break the high symmetry of Fe–N–C and modulate the adsorption strength of the intermediate to a moderate state, manifesting robust cycling stability for over 580 cycles.[13] Hence, it is necessary to direct carbon materials (such as carbon layers, carbon nanotubes, or carbon dots) into TMOs to mitigate polarization losses associated with electrical resistance and optimize binding with reaction intermediates. Additionally, in our previous work, it was proved that the surface of a nanoporous (np) TMO is rich in low-coordination atoms and defects, which are conducive to tight binding with its loadings or coatings.[14–16] Therefore, it can be speculated that cladding carbon onto dealloying-derived np-TMOs may be more stable than that onto flat TMOs due to the high roughness of the former.

Furthermore, numerous studies have revealed that encapsulating small amounts of precious metals (PMs) onto a TMO could not only increase the utilization efficiency of PMs, but also significantly improve catalytic activity and stability. For instance, regulating metal–support interactions between Pt NPs (0.01 mg cm^{-2}) and a $[Ti_2O]^{2+}\cdot 2e^-$ support can indeed strengthen the durability of an integrated electrode and manifest 89 times higher ORR activity than that of commercial Pt/C. Simultaneously, the enriched electrons on the surface of the catalyst had effectively impeded the generation of a pernicious Pt–O layer in alkaline media.[17] Li's group[18] reported that Pt and Pd exhibited significant encapsulation phenomena on TiO_2, owing to the high affinity of metal components in metal oxides, that is the formation of metal–metal interactions among PMs and supports. In addition, CeO_2 and ZrO_2 were also reversible supports that could be used for PM encapsulation. Gong *et al.*[19] discovered that the mass loading of PtSnCu on Al_2O_3 was 0.03 wt%, while a catalytic performance 2–3 times that of industrial PtCu/Al_2O_3 (PtSn loading: 0.3 wt%) could be achieved. This is mainly because the strong Pt–Sn interaction could capture Pt atoms from the Cu lattice and ensure the exposure rate of metallic Pt could reach 100%. Based on these, combining a small amount of PM with a carbon-encapsulated np-TMOs support is helpful for utilizing the advantages of both, achieving dual-function activity and cycle stability.

Herein, we propose a "dealloying–carbon coating–dip pyrolysis" strategy for the highly stable loading of a small amount of Pt nanoparticles (0.032 mg cm^{-2}) onto a carbon-encapsulated nanoporous spinel. It should be noted that the medial carbon layer could not only play a bridging role between np-CFO and Pt, but also lead to the loading of more zero-valence Pt. In view of its nanoporous structure with a larger specific surface area, an adhered carbon layer with superior electrical conductivity, np spinel carriers with OER properties and Pt nanoparticles with ORR performance, the resultant Pt/np-CFO@C exhibits an ORR half-wave potential of 0.86 V, an OER potential of 1.56 V at 10 mA cm^{-2} and a lower ΔE of 0.7 V. Theoretical calculation reveals that Pt/CFO@C possesses metallic properties, a stable adsorption/desorption interface and the lowest energy barrier for ORR/OER. A Pt/np-CFO@C-based ZAB delivers a specific capacity of 781 mA h g^{-1}, a power density of 185 mW cm^{-2} and a cycling life exceeding 1400 hours. This work provides constructive insights into the development of aqueous batteries through the design of cost-effective catalysts.

Results and discussion

Phase and microstructure analysis

As illustrated in Fig. 1a, a Pt/np-CFO@C electrode was prepared by alloying–dealloying–carbon coating–dip pyrolysis. In this, the first step (alloy–dealloying) is helpful for obtaining a porous carrier and providing abundant places for subsequent carbon encapsulation and Pt loading. The second step (carbon coating) has multiple effects, such as improving electrical conductivity, reducing the degree of oxidation of the carrier, and increasing the amount of Pt loading. The last step (dip pyrolysis) could not only realize fast Pt loading, but also guarantee the higher purity of Pt.

As shown in Fig. 1b1, the dealloying-derived porous carrier could fully match the X-ray diffraction (XRD) peaks of the $CoFe_2O_4$ phase (PDF#01-079-1744), demonstrating that the dealloying strategy could spontaneously produce the relevant oxide even at room temperature.[20] After carbon coating (Fig. 1b2), the corresponding phase has transformed into $Fe_{11}Co_5$ (PDF#01-075-7978), for which the atomic ratio of Fe to Co is still 2 : 1, while the oxygen element has disappeared. Learning from the details of the foregoing synthesis, it is found that the carbon coating process is conducted under the conditions of a high vacuum and high temperature, under which the carbon layer could plunder the oxygen atoms of the np-CFO carrier to produce gas (CO_2/CO) to overflow. Additionally, a characteristic peak of C (002) can also be observed, proving the successful introduction of carbon. As for Pt-loaded products, such as Pt/np-CFO and Pt/np-CFO@C (Fig. 1b3 and b4), there simultaneously appear a CFO peak and a Pt peak (PDF#04-004-8733). Interestingly, the Pt peak intensity of Pt/np-CFO@C is significantly stronger than that of Pt/np-CFO, which indicates that carbon-encapsulated CFO is more beneficial to loading Pt element. While the return of oxygen atoms in Pt/np-CFO@C may be ascribed to the unstable oxygen vacancies formed in the np-CFO@C support that are prone to backfilling. From the ICP results in Table S1, the Pt content of Pt/np-CFO@C (5.09%) is greater than that of Pt/np-CFO (4.45%), which is consistent with the above XRD results.

Open Access Article. Published on 12 January 2026. Downloaded on 5/6/2026 12:28:05 AM.
This article is licensed under a Creative Commons Attribution-NonCommercial 3.0 Unported Licence.

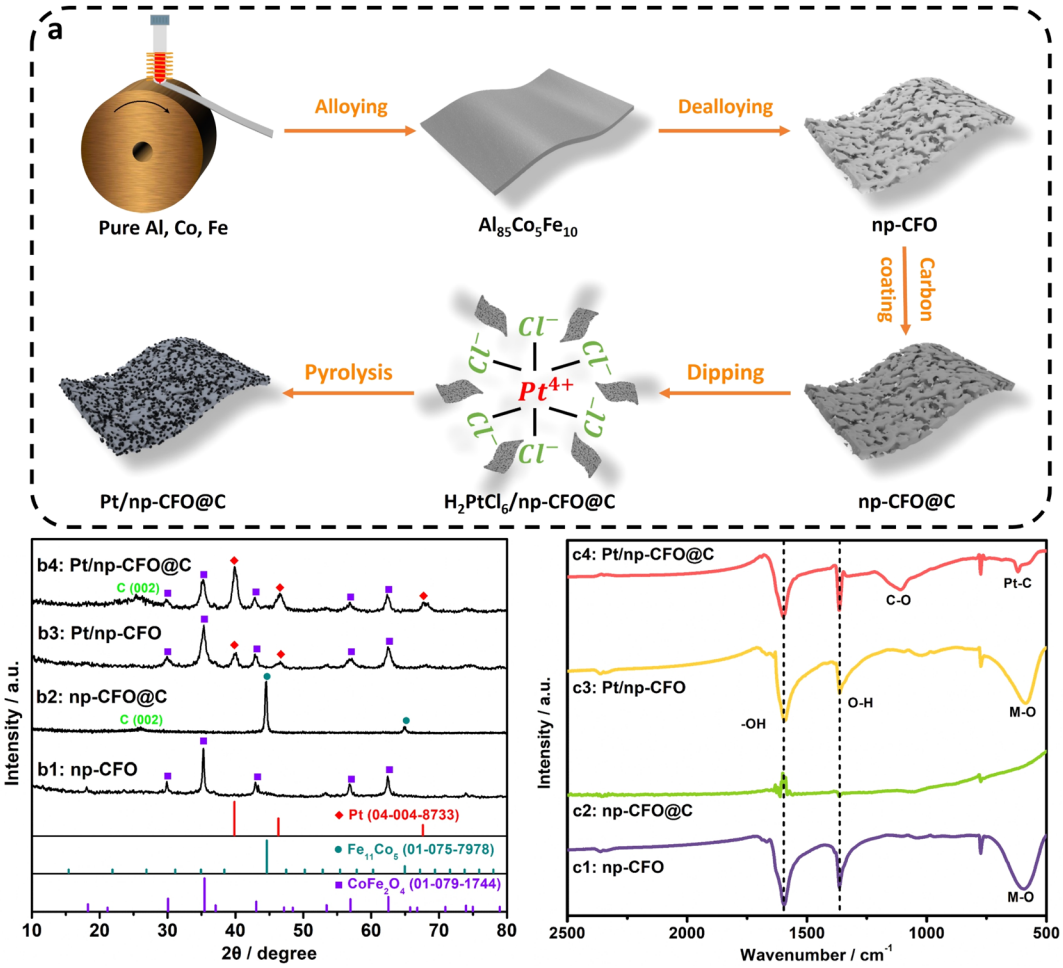

Fig. 1 (a) Preparation process of the Pt/np-CFO@C electrode. XRD patterns of (b1) np-CFO, (b2) np-CFO@C, (b3) Pt/np-CFO and (b4) Pt/np-CFO@C. FTIR spectra of (c1) np-CFO, (c2) np-CFO@C, (c3) Pt/np-CFO and (c4) Pt/np-CFO@C.

Furthermore, the Fourier transform infrared (FTIR) spectra in Fig. 1c1–c3 demonstrate that the metal–O bond at *ca.* 590 cm^{-1} has indeed disappeared when the np-CFO carrier is coated with a carbon layer, but not for Pt/np-CFO.[21] This result reconfirms that the vacuum carbonization process could remove O atoms from the np-CFO carrier, which is consistent with the XRD results. As for Pt/np-CFO@C (Fig. 1c4), a Pt–C bond and a C–O bond can be detected at 620 cm^{-1} and 1115 cm^{-1}, respectively,[22] indicating that the carbon layer plays a bridging role between np-CFO and Pt. On the one hand, the carbon layer could reinforce the anchoring of Pt *via* Pt–C bonds and enhance its ORR activity. On the other hand, the carbon layer could improve the electrical conductivity of np-CFO *via* C–O bonds and boost its OER activity. Moreover, the O–H bond at 1365 cm^{-1} and –OH bond at 1600 cm^{-1} can be detected in all four catalysts, demonstrating that the np-CFO carrier is enriched in hydroxyl that may be conducive to oxygen adsorption/desorption.

As can be observed from Fig. 2a and S1a, np-CFO possesses a typical porous-ligament structure, on which there are also distributed some nanosheets that may be ascribed to dealloying of Al in air, providing abundant places for electro-catalytic reactions or subsequent Pt loading. After carbon coating (np-CFO@C), it is found that there is indeed a cladding layer of material on the surface of np-CFO, but the ligament profile is simultaneously maintained (Fig. 2b and S1b), proving successful coating by carbon. Based on np-CFO@C, Pt loading in a vacuum environment could not only tightly anchor a large number of Pt NPs but also again open the porous channels, as shown in Fig. 2c and S1c. Fig. S1d shows that Pt NPs are also fixed onto the surface of np-CFO, but they are larger, uneven and unstable compared to those on np-CFO@C. Hence, constructing carbon bridge engineering between np-CFO and Pt NPs plays a key role in Pt loading, such as size, uniformity and stability. Furthermore, elemental mappings of the Pt/np-CFO@C electrode in Fig. 2d demonstrate that Co, Fe, O, C and residual Al elements are evenly distributed on the surface of the ligaments, while Pt element spreads over both the pores and ligaments. This phenomenon laterally confirms that porous carriers could definitely increase the loading quantities of Pt.

When magnifying a local region of Pt/np-CFO@C, some large-sized Pt NPs and a large amount of uniformly dispersed small-sized Pt can be simultaneously observed (Fig. 2e). Further focusing on a large Pt particle, Fig. 2f shows a well-shaped

© 2026 The Author(s). Published by the Royal Society of Chemistry

Open Access Article. Published on 12 January 2026. Downloaded on 5/6/2026 12:28:05 AM. This article is licensed under a Creative Commons Attribution-NonCommercial 3.0 Unported Licence.

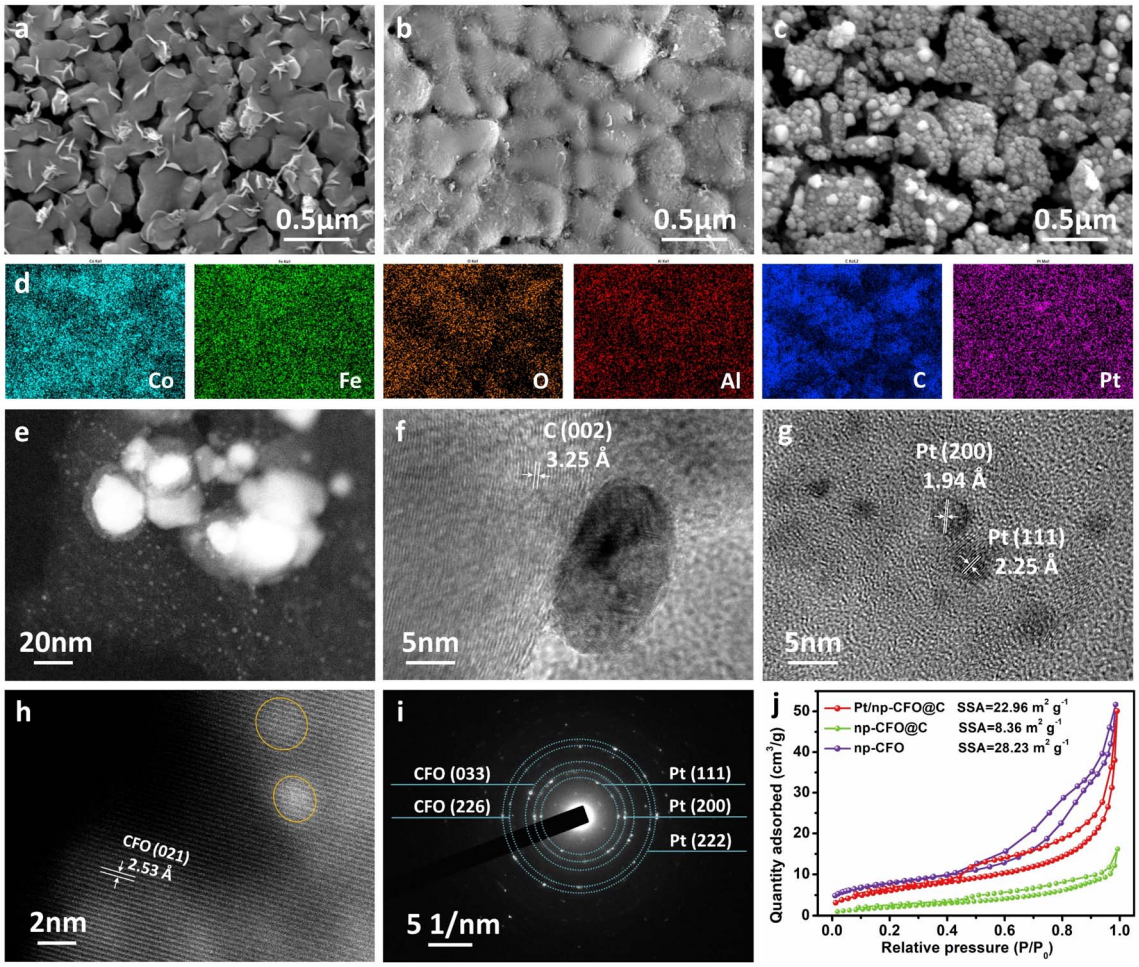

Fig. 2 SEM images of (a) np-CFO, (b) np-CFO@C and (c) Pt/np-CFO@C electrodes. (d) Corresponding elemental mapping of Pt/np-CFO@C. (e–g) TEM and HRTEM images of Pt/np-CFO@C. (h) A HAADF image of Pt/np-CFO@C. (i) The SAED pattern of Pt/np-CFO@C. (j) N_2 sorption isotherms of np-CFO, np-CFO@C and Pt/np-CFO@C electrodes.

nanosphere (*ca.* 15–20 nm) anchored at the surface of the carbon layer (3.25 Å). As for the small-sized Pt NPs, the diameters are all less than 5 nm and the interplanar distances correspond to Pt (111) and Pt (200), respectively (Fig. 2g). It is worth noting that only the lattice fringes of $CoFe_2O_4$ (021) can be measured, but not of those of Pt in some regions (Fig. 2h), which may be ascribed to the post-formed oxide layer that has covered the surface of Pt. This protective layer has been reported to be capable of forming strong metal–support interaction (SMSI) with Pt, which could significantly enhance the stability of a loaded electrode.[23,24] It can be deduced from this that the dispersed smaller Pt nanoparticles would offer more active sites and ensure overall stability. From the selected area electron diffraction (SAED) rings in Fig. 2i, $CoFe_2O_4$ (033), $CoFe_2O_4$ (226), Pt (111), Pt (200) and Pt (222) can be detected, reconfirming the strong interactions between precious metals and porous carriers.

In Fig. 2j and S2, the N_2 sorption isotherms and pore size distribution curves indicate the mesoporous characteristics of np-CFO, np-CFO@C and Pt/np-CFO@C. Among them, Pt/np-CFO@C possesses a specific surface area (SSA) of 22.96 m^2 g^{-1} and pore volume of 0.076 mL g^{-1}, which are much larger than those of np-CFO@C (8.36 m^2 g^{-1}, 0.023 mL g^{-1}) but slightly lower than those of np-CFO (28.23 m^2 g^{-1}, 0.079 mL g^{-1}). For the former, this may be because the coating carbon layer has blocked the channels/pores of np-CFO. For the latter, it stems from the reopening of porous channels during the pyrolysis of H_2PtCl_6, which is consistent with the SEM results in Fig. 2(a and b). Despite this, this strategy still introduces more active sites into a Pt/np-CFO@C electrode, which exhibits the highest electrochemically active surface area (ECSA) among all the catalysts (shown in Fig. 4e). It is worth noting that the SSA values of these porous metal materials are generally lower than those of some other carbon-based materials, which are mainly derived from their larger specific gravities.

X-ray photoelectron spectroscopy (XPS) measurements are used for analyzing the element valence states of Pt/np-CFO@C and Pt/np-CFO.[25] When comparing the full scans of both (Fig. S3a and b), a stronger C 1s signal of Pt/np-CFO@C can be observed, proving the existence of the carbon layer within it. In the high-resolution spectrum of Co 2p for Pt/np-CFO@C (Fig. 3a), the peaks at 780.8 and 796.2 eV are consistent with

Open Access Article. Published on 12 January 2026. Downloaded on 5/6/2026 12:28:05 AM.
This article is licensed under a Creative Commons Attribution-NonCommercial 3.0 Unported Licence.

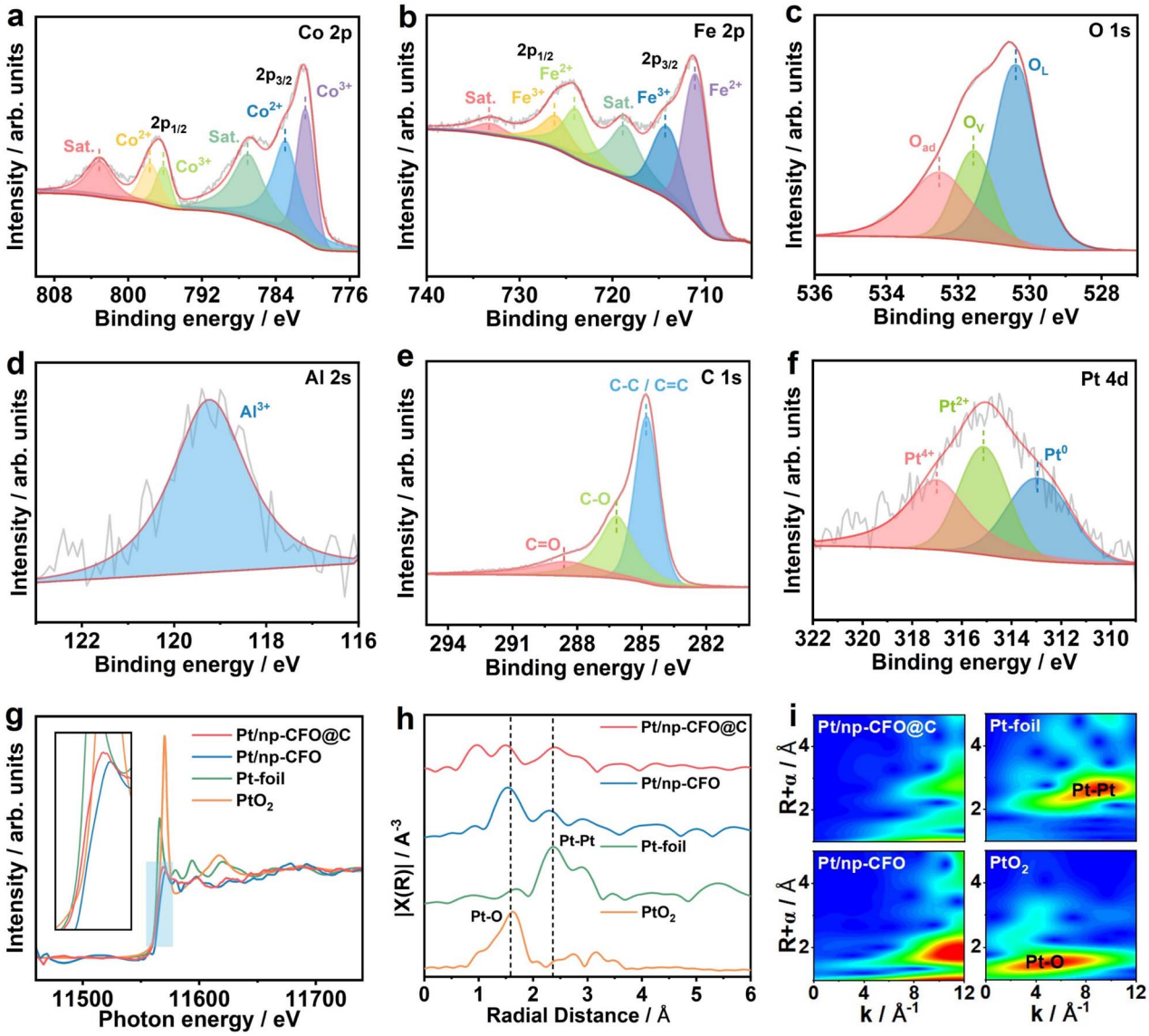

Fig. 3 XPS spectra of the Pt/np-CFO@C electrode: (a) Co 2p, (b) Fe 2p, (c) O 1s, (d) Al 2s, (e) C 1s and (f) Pt 4d. (g) Pt L_3-edge XANES spectra of Pt/np-CFO@C, Pt/np-CFO, Pt foil and PtO_2. (h) Pt L_3-edge EXAFS spectra of Pt/np-CFO@C, Pt/np-CFO, Pt foil and PtO_2. (i) Pt L_3-edge WT-EXAFS signals of Pt/np-CFO@C, Pt/np-CFO, Pt foil and PtO_2.

the binding energies (BEs) of Co^{3+}, while the two peaks at 782.9 and 797.7 eV belong to the states of Co^{2+}.[26,27] In the Fe 2p spectrum (Fig. 3b), the peaks at 711.1 and 724.1 eV are attributed to Fe^{2+}, while the signals at 714.3 and 726.2 eV along with a pair of satellite peaks represent Fe^{3+}.[28,29] The O 1s region in Fig. 3c can be split into three peaks: a lattice oxygen (O_L) peak at 530.4 eV, an oxygen vacancy (O_v) peak at 531.5 eV and an adsorbed oxygen (O_{ad}) peak at 532.5 eV.[30] Here, O_L is the dominant peak, demonstrating that np-CFO could possess better crystallinity through a simple alloying–dealloying strategy.

In Fig. 3d, Al^{3+} can be detected even after complete dealloying,[31] indicating that Al element could indeed remain in host porous materials and it can be doped *in situ* into them to optimize their electronic structures. As for Pt/np-CFO (Fig. S3c–f), the Co 2p, Fe 2p, O 1s and Al 2s signal peaks are similar to those of Pt/np-CFO@C. The difference is that C 1s in Pt/np-CFO@C can be decomposed into a C–C/C=C peak at 284.8 eV, a C–O peak at 286.2 eV and a C=O peak at 288.6 eV,[32,33] among which the area of the C–C/C=C peak is the largest (Fig. 3e), reconfirming the important role of the carbon layer in the Pt/np-CFO@C catalyst. In the Pt 4d region, the BE located at 312.9, 315.1 and 317.0 eV are assigned to Pt^0, Pt^{2+} and Pt^{4+}, respectively.[34] Interestingly, the Pt^0 peak area ratio of Pt/np-CFO@C (35.22%, Fig. 3f) is significantly greater than that of Pt/np-CFO (21.75%, shown in Fig. S3g and Table S2), reflecting the fact that pure Pt is inclined to be loaded on the surface of np-CFO@C. In other words, carbon-encapsulated CFO is more conducive to loading Pt element.

The local coordination environment and electronic structure of Pt atoms are investigated by X-ray absorption fine structure (XAFS). Fig. 3g shows the X-ray absorption near-edge structure

© 2026 The Author(s). Published by the Royal Society of Chemistry

Open Access Article. Published on 12 January 2026. Downloaded on 5/6/2026 12:28:05 AM. This article is licensed under a Creative Commons Attribution-NonCommercial 3.0 Unported Licence.

(XANES) of Pt L_3-edge in Pt/np-CFO@C, Pt/np-CFO, Pt foil and PtO_2. It is found that the absorption edge of Pt/np-CFO@C is located between those of Pt foil and PtO_2, showing that there is a portion of zero-valent platinum and another portion of four-valent platinum.[35] Whereas for Pt/np-CFO, its absorption edge position is far away from that of Pt foil, indicating that the proportion of Pt^0 is relatively low. Notably, the intensities of the white line for Pt/np-CFO@C and Pt/np-CFO are significantly weaker than those of Pt foil (Pt^0) or PtO_2 (Pt^{4+}), which is mainly because the stronger inherent X-ray absorption of the CFO supports has masked the intensity of Pt signals of the two home-made catalysts. But after zooming in to the region of the white line, enhanced intensity for Pt/np-CFO@C can be observed relative to Pt/np-CFO, which results from electron transfer from the Pt 5d orbitals to the middle carbon layer.[36] In other words, the carbon layer could effectively promote electron conduction and enhance the metal–support interaction (MSI).

The local coordination environment of Pt was further probed by Fourier-transformed extended X-ray absorption fine structure (FT-EXAFS) in *R*-space (Fig. 3h). It can be clearly observed that the peak area of Pt–Pt (2.36 Å) is larger than that of Pt–O (1.58 Å) for Pt/np-CFO@C, while the former is far weaker than the latter for Pt/np-CFO, in agreement with the results of Fig. 3g. This again explains why there are more Pt^0 and less Pt^{4+} in Pt/np-CFO@C, while the proportion in Pt/np-CFO is the opposite. Furthermore, the corresponding wavelet transformed (WT) EXAFS was performed to better resolve overlapping coordination signals. In Fig. 3i, the intensity maximum for Pt/np-CFO@C is distributed in the range $k \approx 8$–12 Å^{-1} and $R \approx 2.2$–3.7 Å. This feature has a higher degree of overlap to that of Pt foil ($k \approx 6$–11 Å^{-1}, $R \approx 2.2$–3.0 Å), indicating that the local structure of Pt/np-CFO@C is predominantly governed by Pt–Pt bonds. In comparison, the intensity maximum for Pt/np-CFO shifts to a lower *R*-space ($\approx$1.5–2.3 Å) while retaining intensity at higher *k*-space ($\approx$8–12 Å^{-1}). This pattern is a clear combination of contributions from the Pt–O bonds in PtO_2 ($k \approx 1$–9 Å^{-1}, $R \approx 1.2$–1.8 Å) and the Pt–Pt bonds in Pt foil, with Pt–O coordination making a relatively more pronounced contribution.[37] All these results reflect the fact that the middle carbon layer in Pt/np-CFO@C is conducive to loading more zero-valence Pt, which is an active element for the ORR activity or discharge performance of ZAB.

Electrocatalytic performance analysis

The OER performances of Pt/np-CFO@C, np-CFO@C, Pt/np-CFO, np-CFO and commercial RuO_2 are systematically evaluated in 1 M KOH. As exhibited in Fig. 4a and b, Pt/np-CFO@C possesses a higher overpotential of 329 mV at 10 mA cm^{-2} than that of RuO_2, but the lowest overpotentials of 397 and 457 mV at 50 and 100 mA cm^{-2}, respectively. It has also outperformed the OER activities of np-CFO@C, Pt/np-CFO, np-CFO and some other reported catalysts (Table S4).[38–40] The Tafel plots in Fig. 4c, derived from the corresponding LSV curves, provide insight into the OER kinetics of the catalysts. A lower Tafel slope corresponds to more favorable reaction kinetics.[41] Accordingly, the Pt/np-CFO@C composite exhibits a lower Tafel slope of 79.8 mV dec^{-1}, indicating a smaller increase in overpotential with rising current density and thus superior catalytic kinetics.

Electrochemical impedance spectroscopy (EIS) was conducted at 1.5 V to probe the charge transfer properties of the catalysts.[42] The Nyquist plots in Fig. 4d, modeled with equivalent circuits, reveal that Pt/np-CFO@C exhibits a lower charge-transfer resistance (R_{ct}) of 37.2 Ω (Table S3). This is attributed to the intermediate carbon layer, which disrupts the inherent charge distribution and thereby facilitates more efficient charge transfer. Notably, Pt/np-CFO possesses the smallest value for R_{ct}, which can also be seen from the electronic density of states (DOS) in Fig. 5, mainly derived from the poor symmetry of up-spin and down-spin that may be unfavorable for the stable adsorption of intermediates. The ECSA of the catalysts can be estimated from their double-layer capacitance (C_{dl}), as shown in Fig. 4e. Cyclic voltammetry (CV) should first be performed in a non-faradaic potential window (1.0–1.1 V *vs.* RHE) at various scan rates (5–100 mV s^{-1}, Fig. S4a–d). Then, the C_{dl} values are obtained by plotting half the current density difference ($\Delta j/2$) at 1.05 V against the scan rate. Finally, the C_{dl} for Pt/np-CFO@C is calculated to be 63.2 mF cm^{-2}, which corresponds to an ECSA of approximately 1580 cm^2 according to eqn (S8).[43] This ECSA value is substantially larger than those of np-CFO@C (355 cm^2), Pt/np-CFO (537.5 cm^2), or np-CFO (585 cm^2). Furthermore, the operational durability of Pt/np-CFO@C has been evaluated by chronopotentiometry (CP) at a constant current density of 100 mA cm^{-2}. As shown in Fig. 4f, the electrode potential exhibits a slight decline of 82 mV after 200 hours of testing, indicating enhanced activation over time. The stability of Pt/np-CFO@C is verified further by an accelerated degradation test (ADT), where the E_{200} for OER increases by only 10 mV after 5000 continuous CV cycles (inset to Fig. 4f), confirming its superior stability. The remarkable durability and stability may be attributed to the intermediate carbon layer, which not only facilitates effective bridging between the np-CFO support and Pt nanoparticles, but also possesses robust structural integrity.

The ORR activities of Pt/np-CFO@C, np-CFO@C, Pt/np-CFO, np-CFO and benchmark commercial Pt/C are evaluated using a rotating disk electrode (RDE) at 1600 rpm in O_2-saturated 0.1 M KOH (Fig. 4g and h). Among the synthesized catalysts, Pt/np-CFO@C demonstrates superior ORR activity, exhibiting a half-wave potential ($E_{1/2}$) of 0.86 V and a limiting current density (j_L) of 5.69 mA cm^{-2}. These values are higher than those of np-CFO@C (0.75 V, 4.96 mA cm^{-2}), Pt/np-CFO (0.67 V, 4.15 mA cm^{-2}), np-CFO (0.47 V, 3.37 mA cm^{-2}), or Pt/C (0.85 V, 5.41 mA cm^{-2}) and are comparable to those of other reported ORR catalysts (Table S5).[44,45] The Tafel analysis in Fig. 4i further corroborates the faster kinetics of Pt/np-CFO@C for ORR, which exhibits a slope of 65.4 mV dec^{-1}. This is attributed mainly to the high conductivity of the medial carbon layer and the high utilization rate of Pt nanoparticles, synergistically providing abundant and effective active sites for ORR.

To determine the intrinsic electron transfer number (n) for ORR on Pt/np-CFO@C, Koutecky–Levich (K–L) analysis has been employed. The K–L plots (Fig. S4f), derived from LSV curves measured at various rotation rates (400–2500 rpm, Fig. S4e), yield an n value of 3.8, indicating that it proceeds

Open Access Article. Published on 12 January 2026. Downloaded on 5/6/2026 12:28:05 AM.
This article is licensed under a Creative Commons Attribution-NonCommercial 3.0 Unported Licence.

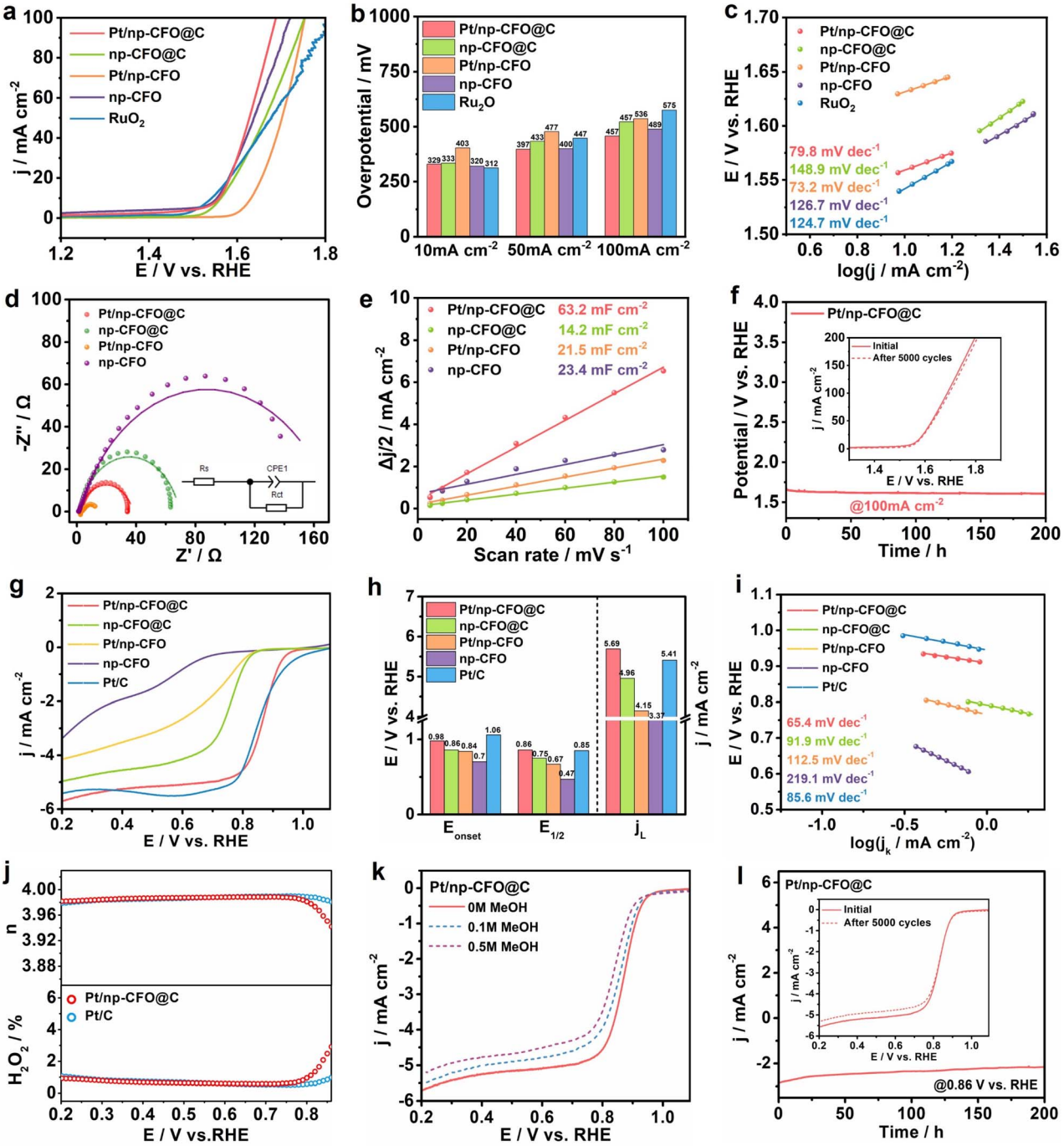

Fig. 4 OER performances: (a) LSV curves; (b) a comparison of η_{10}, η_{50} and η_{100}; (c) Tafel slopes; (d) Nyquist plots; (e) C_{dl} values; and (f) the CP profile at 100 mA cm^{-2}; the inset shows LSV curves of Pt/np-CFO@C before and after ADT. ORR performances: (g) LSV curves; (h) a comparison of E_{onset}, $E_{1/2}$ and j_L; (i) Tafel slopes; (j) electron transfer numbers and H_2O_2 yields on Pt/np-CFO@C and Pt/C derived from RRDE testing; (k) methanol tolerance of Pt/np-CFO@C; and (l) the CA profile at 0.86 V *vs.* RHE; the inset shows LSV curves of Pt/np-CFO@C before and after ADT.

predominantly *via* an efficient four-electron pathway. Using RRDE testing, the electron transfer number and hydrogen peroxide yield on Pt/np-CFO@C can be determined to be 3.98 and 0.92%, respectively, which are very close to those for benchmark Pt/C (Fig. 4j). For high-performance ORR catalysts, it is imperative to assess their tolerance to poisoning by small molecules, such as methanol (MeOH).[46] As shown in Fig. 4k, the LSV curves of Pt/np-CFO@C manifest only a minor negative shift while retaining their original shape upon the introduction of 0.1 M or 0.5 M MeOH, indicating negligible impact. In Fig. S4g, Pt/np-CFO exhibits inferior MeOH tolerance to that of Pt/np-CFO@C, owing to the absence of a middle carbon layer that could reduce the bonding strength of the CFO support and Pt NPs. In stark contrast, Pt/C suffers from a pronounced poisoning effect under the same conditions, which leads to complete inactivation of its active sites and severe distortion of

© 2026 The Author(s). Published by the Royal Society of Chemistry

Open Access Article. Published on 12 January 2026. Downloaded on 5/6/2026 12:28:05 AM. This article is licensed under a Creative Commons Attribution-NonCommercial 3.0 Unported Licence.

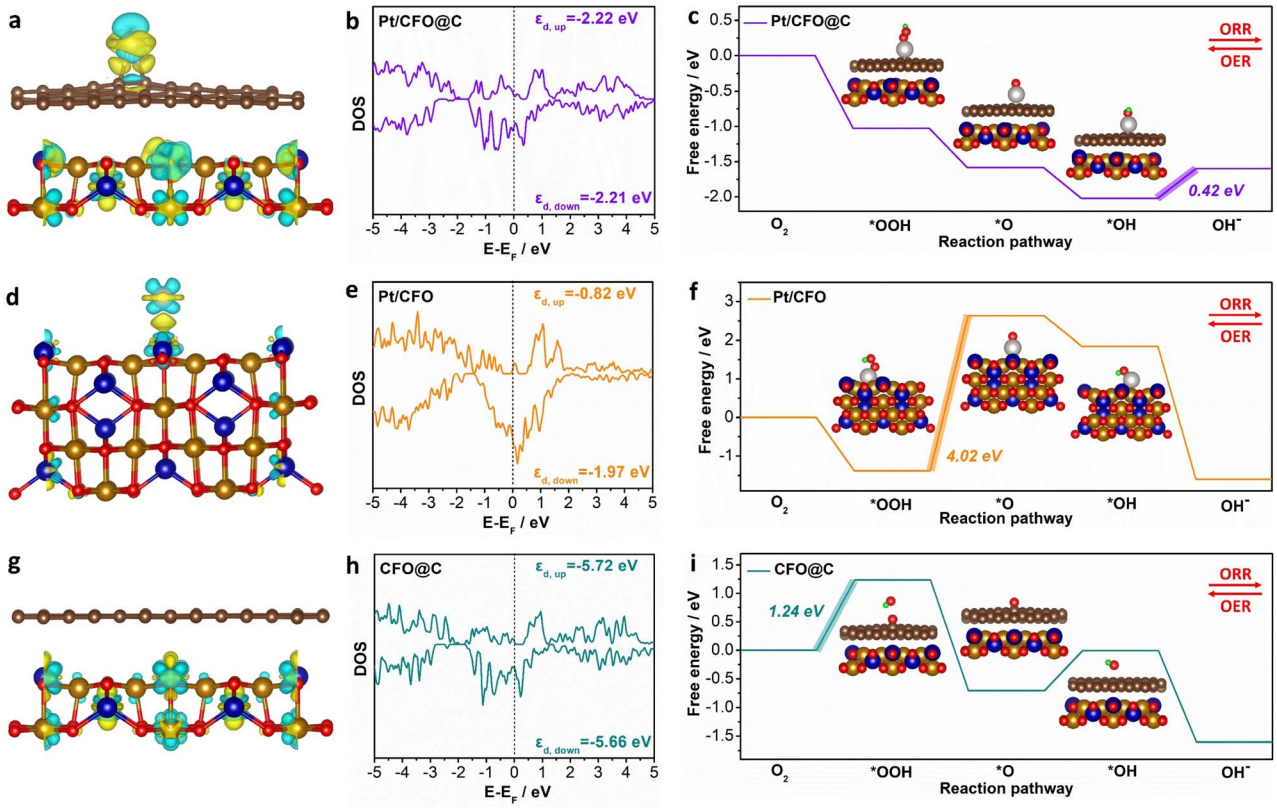

Fig. 5 Distribution of charge density difference on (a) Pt/CFO@C, (d) Pt/CFO and (g) CFO@C; yellow and cyan zones represent electron accumulation and depletion, respectively. (b, e, and h) DOS and corresponding d-band centers. Gibbs free energy of adsorbed *OH, *O, and *OOH on (c) Pt/CFO@C, (f) Pt/CFO, and (i) CFO@C. Blue, light brown, gray, dark brown, red and green balls represent Co, Fe, Pt, C, O and H atoms, respectively.

the LSV curves (Fig. S4h). In other words, the robust anti-poisoning capability of Pt/np-CFO@C offers a distinct advantage in terms of operational stability. Subsequently, the stability of Pt/np-CFO@C is measured by chronoamperometry (CA) and ADT. CA testing shown in Fig. 4l reveals a decay in current density of 0.6 mA cm^{-2}. Following 5000 CV cycles, the $E_{1/2}$ value shows a negligible shift, while the j_L decreased by 0.27 mA cm^{-2}, likely due to slight carbon corrosion during ADT. Overall, this confirms the eminent stability of the Pt/np-CFO@C catalyst.

DFT analysis

As evidenced by the above experimental results, Pt/np-CFO@C exhibits remarkable bifunctional oxygen electrocatalytic activity. In order to unravel the structure–activity relationship at atomic level, we have established three comparative models (Pt/CFO@C, Pt/CFO and CFO@C) to investigate their distinctive electronic configurations and adsorption/desorption energetic profiles toward critical oxygen-containing intermediates.

As shown in Fig. S5, four possible configurations of Pt/CFO@C were set to search for the most stable Pt-loading model. After structural optimization, Pt/CFO@C-2 has been selected as the optimum model for adsorption of oxygen intermediates derived from its lowest total energy ($E_t = -916.23$ eV). As for Pt/CFO, Pt/CFO-1 is more appropriate for subsequent adsorption based on the same rule (Fig. S6). Therefore, Pt/CFO@C-2 (Fig. 5a) and Pt/CFO-1 (Fig. 5d) models can be used directly for the adsorption of *OOH, *O and *OH. But for CFO@C (Fig. 5g), although it is not necessary for the loading of Pt atoms, it is necessary to select a suitable oxygen adsorption model. By contrast, the CFO@C-O-1 model is the most stable *O configuration and can also be regarded as the adsorption sites of *OH and *OOH (Fig. S7).

From the distribution of charge density differences in Fig. 5(a and d), it is found that the middle carbon layer could modify the electron density around the Pt atom. The charge accumulation and depletion on Pt/CFO@C is more even than that on Pt/CFO, which leads to intermediates being easily adsorbed on (or desorbed from) the surface of Pt/CFO@C and then promotes faster ORR/OER.[47] As for CFO@C (Fig. 5g), although there is electron transfer within the CFO support, there is not between CFO and the C coating, decreasing the catalytic activity of the surface. Subsequently, the density of states (DOS) in Fig. 5(b, e and h) reveals that none of the three models have band gaps at the Fermi level and possess metallic properties, proving that either carbon coating, or Pt loading could provide more valence electrons for $CoFe_2O_4$. Moreover, the d-band center of Pt/CFO@C in up-spin is calculated as −2.22 eV, which is similar to that in down-spin (−2.21 eV), not only demonstrating its stronger adsorption capacity for intermediates,[48] but also reflecting its notable stability due to the

Open Access Article. Published on 12 January 2026. Downloaded on 5/6/2026 12:28:05 AM. This article is licensed under a Creative Commons Attribution-NonCommercial 3.0 Unported Licence.

symmetric d-band centers. Despite the d-band centers of Pt/CFO ($\varepsilon_{d,up} = -0.82$ eV, $\varepsilon_{d,down} = -1.97$ eV) being larger than those of Pt/CFO@C and CFO@C ($\varepsilon_{d,up} = -5.72$ eV, $\varepsilon_{d,down} = -5.66$ eV), its poor symmetry may be unfavorable for the stable adsorption of intermediates.

Based on formulae (S16)–(S19), the Gibbs free energies of ORR on different models can be calculated (Fig. 5c, f and i). As expected, the energy barrier of Pt/CFO@C (0.42 eV) is far lower than that of Pt/CFO (4.02 eV) or CFO@C (1.24 eV), confirming that carbon coating and Pt loading could indeed be conducive to improving the oxygen electrocatalytic activity of CFO. Additionally, the rate-determining step (RDS) of Pt/CFO@C (*OH → OH^-) is completely different from those of Pt/CFO (*OOH → *O) or CFO@C (O_2 → *OOH), showing that ORR on the three models is limited by the last hydrogenation, cleavage of O–O bond and first hydrogenation, respectively. From a converse perspective, the Pt/CFO@C composite also demonstrates the lowest energy barrier for OER among the investigated systems. Taken together, these theoretical and experimental findings are mutually corroborating, collectively demonstrating that CFO modified through carbon encapsulation and platinum loading exhibits exceptional performance as a bifunctional oxygen electrocatalyst.

RZAB performance analysis

To evaluate the practicability of Pt/np-CFO@C, it is necessary to construct RZABs with liquid circulation systems (Experimental section in SI and Fig. S8a).[49,50] The oxygen electrocatalytic activity should first be quantified through the potential gap (ΔE) between OER potential at 10 mA cm^{-2} (E_{10}) and half-wave potential of ORR ($E_{1/2}$), expressed as $\Delta E = E_{10} - E_{1/2}$. Commonly, a smaller ΔE value indicates superior reversibility for oxygen conversion.[51] As demonstrated in Fig. 6a, Pt/np-CFO@C exhibits a lower ΔE of 0.73 V than np-CFO@C (0.82 V), Pt/np-CFO (0.98 V) or np-CFO (1.24 V), confirming its exceptional bifunctional oxygen electrocatalytic capability. In Fig. 6b, the self-assembled Pt/np-CFO@C-based ZAB has an open circuit voltage (OCV) of 1.4 V, which could even increase by *ca.* 0.84% after continuous discharge for 5 h, which is consistent with the value measured by a multimeter (Fig. S8b). Meanwhile, two ZABs in series could light up an LED (2.0 V) in the shape of NUC. Additionally, it also delivers a higher power density of 185.45 mW cm^{-2}, which has surpassed the value of a Pt/C||RuO_2-based device (129.63 mW cm^{-2}) and other catalysts (Fig. 6c and Table S6).[52–54]

In Fig. 6d, Pt/np-CFO@C-based ZAB exhibits output voltages of 1.19 V at 2 mA cm^{-2}, 0.93 V at 20 mA cm^{-2} and 0.77 V at 40 mA cm^{-2}, which are significantly greater than those of a Pt/C||RuO_2-based device. Even after reverting to current densities of 20 mA cm^{-2} and 2 mA cm^{-2}, the corresponding potential variation rates are only 0.84% and 1.07%, respectively, unambiguously indicating its preferable reversibility and rate capability under dynamic operating conditions. According to formula (S9), the specific capacities of the Pt/np-CFO@C-based ZAB can be calculated to be 781.06, 779.39 and 775.49 mA h g^{-1} at 5, 10, and 20 mA cm^{-2} (Fig. 6e), as well as corresponding energy densities of 859.17, 810.57 and 620.39 Wh kg^{-1}, respectively. The values are basically consistent with those of the Pt/C||RuO_2-based device, yet fall notably short of theoretical values due to inherent ohmic losses and kinetic limitations.

As can be seen from Fig. 6f, the Pt/np-CFO@C-based ZAB exhibits a lower charge–discharge voltage gap than that of the benchmark, implying its higher cyclic charge–discharge capacity. In this regard, the durability of Pt/np-CFO@C-based and Pt/C||RuO_2-based RZABs were investigated by galvanostatic charge–discharge (GCD) at a constant current density of 10 mA cm^{-2} with 20 min per cycle (Fig. 6g). To rule out the contribution of a carbon paper (CP) substrate to the stability of the performance, a CP-based device was also measured as a contrast sample. Surprisingly, the charge–discharge voltage gap of the Pt/np-CFO@C-based RZAB gradually decreased within the first 20 hours, and subsequently tended to be stable for nearly 1400 h. This may be derived from the evolution of phases or sizes during charging/discharging, which can be clarified by *in situ* XRD. Whereas for CP-based and Pt/C||RuO_2-based RZABs, the batteries failed after 8 h and 100 h, respectively. From the above results, it can be inferred that the middle carbon layer in Pt/np-CFO@C is crucial for conductivity and Pt loading, to make contributions to long-term cyclic charging and discharging. Therefore, Pt/np-CFO@C is a promising bifunctional oxygen electrocatalyst for an RZAB cathode.

In situ testing analysis

In situ Raman spectra was introduced to record Raman signals during the ORR process (from 1.0 to 0.2 V) to trace the intermediate adsorption states on Pt/np-CFO@C. As shown in Fig. 7a, the Raman spectrum exhibits two distinct peaks at 1352 and 1603 cm^{-1}, which are attributed to the D and G bands of graphitic carbon, respectively.[55,56] Observably, the ratios of the two peaks show almost no change even under different potentials, revealing the preferable structural integrity of the medial carbon layer throughout the ORR process. Characteristic peaks at 686, 1150 and 1519 cm^{-1} are assigned to *OH, $*O_2$ and *OOH adsorption, respectively. As the applied potential decreased from 1.0 V to 0.8 V, the absorption peak of $*O_2$ increased; then the peak gradually disappeared, showing that the adsorbed $*O_2$ has reached its maximum and begun converting to *OOH.[57] Simultaneously, the intensity of the *OOH peak was continuously strengthened as the potential decreased to 0.5 V and then began to decline, not only suggesting that the ORR process on Pt/np-CFO@C follows an associative pathway but also suggesting that the strong adsorption of *OOH onto the electrode surface could lead to breakage of the O–O bond, which is the further reduction of *OOH.[58,59] As for the *OH signal, slightly enhanced peaks can be observed compared to those at open circuit potential (OCP), proving that the O–O bond in *OOH has indeed broken and formed hydroxy. All these results confirm that ORR on Pt/np-CFO@C follows a four-electron associative mechanism, which is consistent with the experimental results from RRDE.

In the above cyclic charge–discharge testing, it is found that the ΔE value of Pt/np-CFO@C has gradually decreased within

© 2026 The Author(s). Published by the Royal Society of Chemistry

Open Access Article. Published on 12 January 2026. Downloaded on 5/6/2026 12:28:05 AM.
This article is licensed under a Creative Commons Attribution-NonCommercial 3.0 Unported Licence.

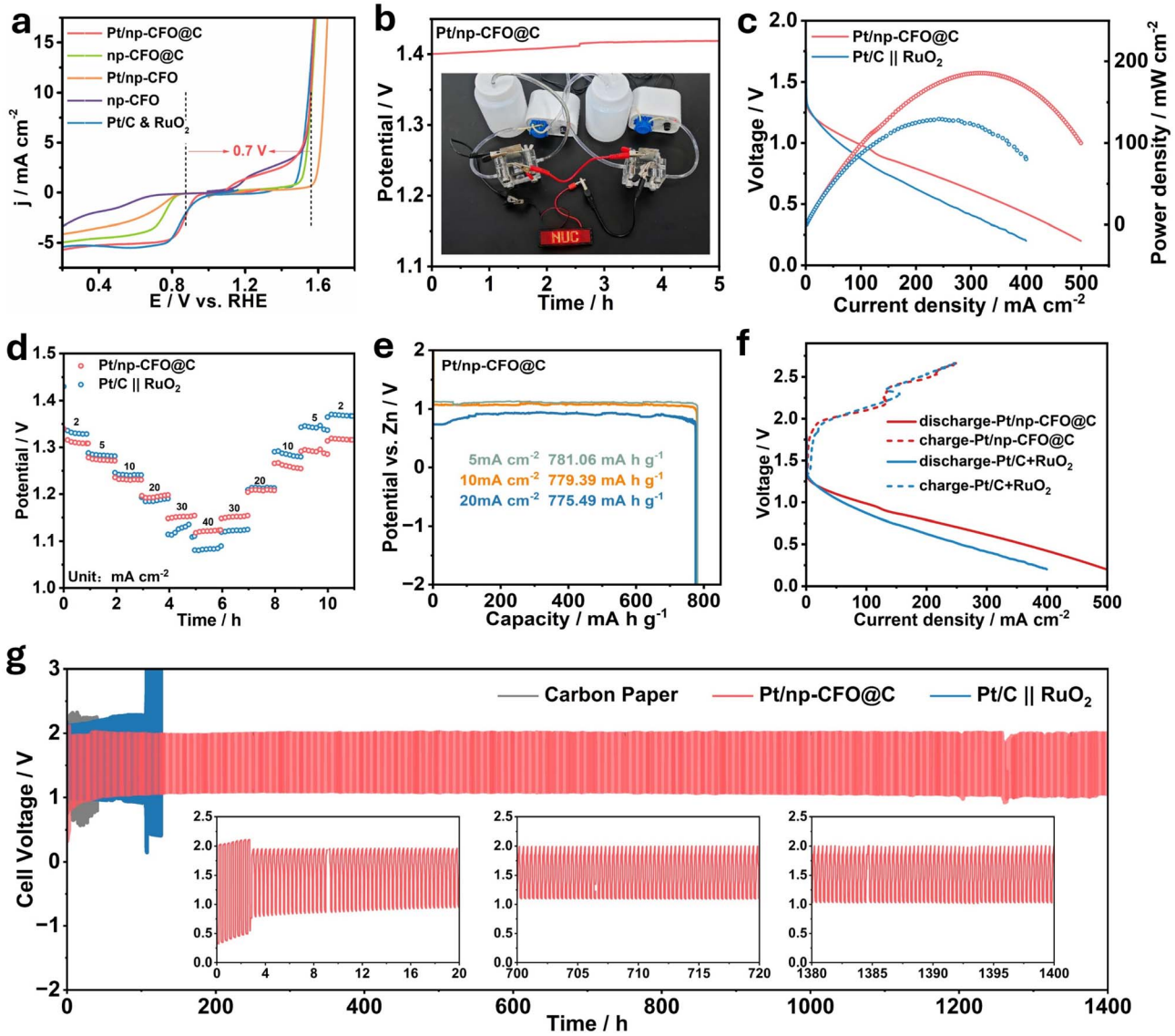

Fig. 6 (a) OER–ORR potential gaps of different samples. (b) Discharge stability at the open circuit potential; the inset shows an LED powered by two Pt/np-CFO@C-based RZABs in series. (c) Discharge polarization curves and power densities of Pt/np-CFO@C-based and Pt/C||RuO_2-based RZABs. (d) Rate capabilities of Pt/np-CFO@C-based and Pt/C||RuO_2-based RZABs. (e) Specific capacity plots of a Pt/np-CFO@C-based RZAB. (f) Charge and discharge polarization curves of Pt/np-CFO@C-based and Pt/C||RuO_2-based RZABs. (g) Cyclic charge–discharge curves of Pt/np-CFO@C-based, carbon-paper-based and Pt/C||RuO_2-based RZABs; the insets show high-resolution outlines at different time periods.

the first 20 hours, which has rarely been found in published work. In other words, the discharge voltage during ORR has increased. To explore and clarify the deep-seated reasons behind this, we use *in situ* XRD, which is composed of a primary diffractometer and a sealed electrolytic cell. The electrolytic cell contains a microcirculatory system to decrease concentration polarization, Zn wire to represent the anode of ZAB and an X-ray-penetrable window to connect the cathode material (Fig. 7b and S9). It should be emphasized that the glassy carbon electrode (GCE) in this device is used to conduct electricity rather than support the catalysts, which are loaded on non-opaque carbon paper.[60] So, during the simulated discharging/ORR process, the evolution of original phases can be dynamically detected by *in situ* XRD as X-rays pass through the Kapton window.

From the XRD patterns of Pt/np-CFO@C before and after testing, no changes can be found, except for the worsening crystallinity of the tested one (Fig. S10a). Hence, it is necessary to record the time-resolved *in situ* XRD patterns of the Pt/np-CFO@C-based ZAB under a constant current discharge at 10 mA cm^{-2}. In Fig. 7c, it is not difficult to see that the width of the Pt (200) peak gradually increases with time. From the corresponding waterfall diagram (Fig. 7d), it can also be observed that the green area is getting wider and wider. According to the Scherrer equation ($D = K\lambda/\beta \cos\theta$), the crystal size is inversely proportional to FWHM (β value), and thus the D value has reduced by *ca.* 40% as discharging proceeds. Meanwhile, the

Open Access Article. Published on 12 January 2026. Downloaded on 5/6/2026 12:28:05 AM.
This article is licensed under a Creative Commons Attribution-NonCommercial 3.0 Unported Licence.

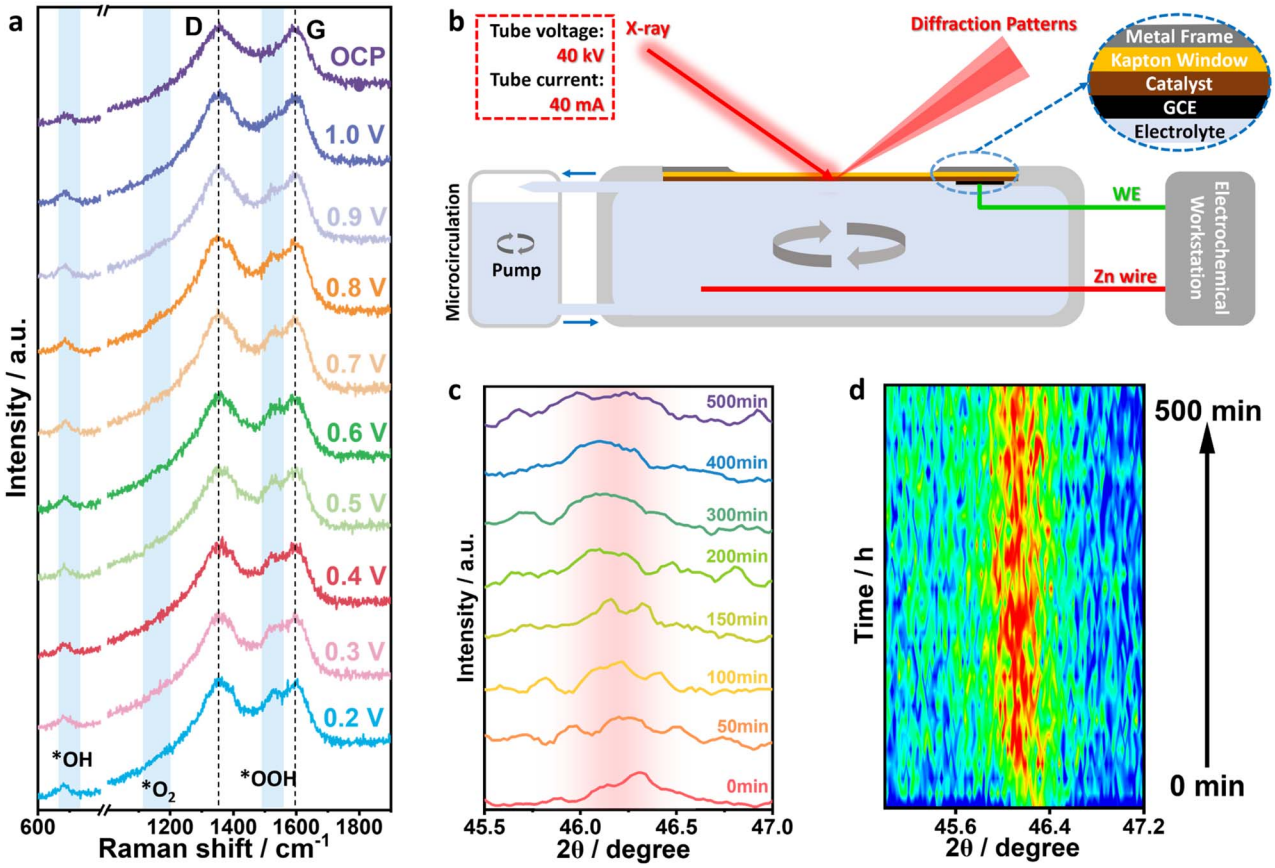

Fig. 7 (a) *In situ* Raman spectra of Pt/np-CFO@C during the ORR. (b) A schematic diagram of an *in situ* X-ray diffractometer applied to a liquid Zn–air battery. (c) Time-resolved *in situ* XRD patterns of a Pt/np-CFO@C-based ZAB during constant current discharge. (d) The corresponding waterfall diagram.

corresponding HRTEM image shown in Fig. S10b also demonstrates that the particle size of tested Pt/np-CFO@C has indeed decreased to 10–15 nm compared to that of the original sample (15–20 nm). The above phenomenon indicates that Pt nanoparticles could become smaller during discharging, which is beneficial for exposing more active sites and showing a gradually improving performance. Moreover, the angle of the Pt (200) peak shifts negatively, arising from the incorporation of impurity atoms that leads to increased interplanar spacing. In short, the decrease in the ΔE value of Pt/np-CFO@C-based ZAB stems mainly from the changes in grain size and lattice spacing during discharging.

Experimental

Similar to our previous study,[19] the nanoporous $CoFe_2O_4$ (np-CFO) carrier was prepared by vacuum melting, melt-spinning and chemical dealloying of $Al_{85}Co_5Fe_{10}$ alloy. Then, 200 mg of np-CFO powder and 800 mg of polyacrylonitrile (PAN) were taken into 5 mL of *N*-methylpyrrolidone (NMP) to obtain a viscous mixture. In order to avoid air pollution, the above mixture was placed into a tube furnace with vacuum degree of 10^{-2} Pa. Meanwhile, the tube should be heated to 250 °C for 2 h, then increased to 700 °C for 2 h and finally naturally cooled to room temperature. The product was named carbon encapsulated np-CFO (np-CFO@C). Finally, 200 mg of np-CFO@C (or np-CFO) were taken into 15 mL of H_2PtCl_6 solution (2 mg mL^{-1}) to form a uniform suspension. In turn, by means of vacuum drying (80 °C, 5 h) and vacuum calcination (500 °C, 2 h), the final product Pt/np-CFO@C (or Pt/np-CFO) was acquired.

Comprehensive details on material characterization, electrochemical testing, the assembly and measurement of Zn–air batteries and computational methods can be found in the SI.

Conclusions

In summary, a "dealloying–carbon coating–dip pyrolysis" strategy was utilized for the highly stable loading of Pt nanoparticles onto carbon-encapsulated porous $CoFe_2O_4$, which is sandwich-like Pt/np-CFO@C. It exhibits an ORR half-wave potential of 0.86 V, an OER potential of 1.56 V at 10 mA cm^{-2} and a lower potential gap (ΔE) of 0.7 V. Meanwhile, a Pt/np-CFO@C-based RZAB delivers a specific capacity of 781 mA h g^{-1}, an energy density of 802 Wh kg^{-1}, a power density of 185 mW cm^{-2} and a cycling life exceeding 1400 hours. FTIR and XAFS results prove that the middle carbon layer is conducive to loading zero-valent Pt onto np-CFO, and simultaneously bridges the two. HAADF imaging proves that the post-formed oxide layer can protect Pt from inactivation through SMSI. *In*

© 2026 The Author(s). Published by the Royal Society of Chemistry

Open Access Article. Published on 12 January 2026. Downloaded on 5/6/2026 12:28:05 AM. This article is licensed under a Creative Commons Attribution-NonCommercial 3.0 Unported Licence.

situ Raman and RRDE testing confirm the 4-electron transfer mechanism of the ORR on Pt/np-CFO@C. DFT calculations verify that Pt/CFO@C has metallic properties, symmetric d-band centers, a notably stable adsorption interface and the lowest energy barrier of 0.42 eV for the ORR. *In situ* XRD reveals that the size of Pt nanoparticles could become smaller during discharging, which is beneficial for exposing more active sites and shows gradually improving performance. Combining experimental and theoretical results, the superior bifunctional activity of Pt/np-CFO@C should be ascribed mainly to the huge surface area of its nanoporous substrate and the bridging effect of the medial carbon layer, in which the former is helpful for facilitating mass/electron transfer, while the latter is able to adjust the electronic structure and allow faster intermediate exchange. This study not only presents a rationally designed bifunctional oxygen electrocatalyst but also lays the groundwork for the advancement of next-generation power sources.

Author contributions

M. W.: conceptualization, writing – original draft, formal analysis, software, funding acquisition. H. D. and Y. N.: investigation, methodology, data curation, validation. G. M. and J. Z.: resources, methodology, writing – review & editing, software. X. W.: resources, methodology. X. L.: resources, supervision, funding acquisition.

Conflicts of interest

There are no conflicts to declare.

Data availability

The authors confirm that the data supporting the findings of this study are available within the article and its supplementary information (SI). Supplementary information: details of experimental procedures, additional experimental results, additional theoretical calculation results and Tables S1–S6. See DOI: https://doi.org/10.1039/d5sc09967f.

Acknowledgements

This work was supported by Central Guidance Fund for Local Science and Technology Development (No. YDZJSX2024D035), Special Fund for Science and Technology Innovation Teams of Shanxi Province (No. 202304051001029) and Scientific and Technological Achievements Transformation Guidance Project of Shanxi Province (No. 202204021301048).

Notes and references

1 S. Sarsenov, C. J. Moon, R. A. Senthil, A. Kumar, V. Maheskumar, M. Ubaidullah, K. Kanjanapaparkul, S. Kheawhom and M. Y. Choi, *Energy Storage Mater.*, 2025, **81**, 104507.
2 C. Zhang, Q. Zhao, J. Wu, F. Guo, Y. Yin, X. Zheng, Y. Ma, F. Gong, J. Liu and W. Wang, *Adv. Funct. Mater.*, 2025, e15095.
3 F. Wang, X. He, G. Qu, M. Mamoor, Y. Zhai, L. Wang, B. Wang, Z. Jing, Y. Kong, D. Wang, L. Kong and L. Xu, *ACS Nano*, 2025, **19**, 22330–22342.
4 Z. Chen, L. Zhong, Z. Chen, H. Zhuo, X. Zhao, H. Lai, T. Li, W. Yang, Z. Liu and H. Zhang, *ACS Nano*, 2025, **19**, 23859–23868.
5 Z. Xu, W. Chen, G. Liu, Y. Sun, X. Qiu, P. Gao, D. Su and M. Shao, *Chem. Eng. J.*, 2025, **515**, 163536.
6 X. Liu, Z. Wang, J. Wang, T. Tang, C. Li, J. Yu, S. Zhang and C. Deng, *Energy Storage Mater.*, 2024, **65**, 103184.
7 Y. Ran, C. Xu, D. Ji, H. Zhao, L. Li and Y. Lei, *Nano Res. Energy*, 2024, **3**, e9120092.
8 S. Kumar and Y.-P. Fu, *J. Colloid Interface Sci.*, 2025, **700**, 138328.
9 K. Li, Y. Li, X. Han, Q. Shao and Z. Lü, *Energy Storage Mater.*, 2025, **78**, 104289.
10 L. Qiao, W. Liu, N. Du, Y. Wang, Y. Li, H. wu and Z. Bao, *Chem. Eng. J.*, 2024, **502**, 157924.
11 J. Peng, F. Liu, X. Huang, L. Feng, H. Wang, X. Wang, J. Ren and R. Wang, *Chem. Eng. J.*, 2025, **511**, 162093.
12 Y. Chen, J. Li, Y. Chen, Y. Cheng, X. Tian, D. Xiao, H.-T. Wang, Y.-R. Lu, L. Zhang, W. Lin, J. Luo and L. Han, *J. Colloid Interface Sci.*, 2025, **686**, 96–106.
13 K. Wei, F. Yang, Y. Sun, C. Yu, J. An, G. Ma and Y. Li, *Adv. Funct. Mater.*, 2025, **35**, 2422039.
14 M. Wang, H. Du, H. Zhao, Y. Cao, R. Dong, H. Wang and H. Hou, *ACS Sustainable Chem. Eng.*, 2023, **11**, 9478–9488.
15 B. Sun, W. Zhang, M. Zheng, J. Meng, L. Liu, G. Ma, Q. Yao and M. Wang, *Inorg. Chem.*, 2024, **63**, 18162–18172.
16 M. Wang, Y. Long, H. Zhao, W. Zhang, L. Wang, R. Dong, H. Hou, H. Wang and X. Wang, *ChemSusChem*, 2022, **15**, e202201518.
17 E. Hua, S. Choi, S. Ren, S. Kim, G. Ali, S. J. Kim, W.-S. Jang, S. Joo, J. Zhang, S. Ji, Y. S. Cho, J. Kang, T. Song, S. Hong, H. Choi, Y.-M. Kim, H. Han and S. W. Kim, *Energy Environ. Sci.*, 2023, **16**, 4464–4473.
18 T. Wang, J. Hu, R. Ouyang, Y. Wang, Y. Huang, S. Hu and W. X. Li, *Science*, 2024, **386**, 915.
19 G. Sun, R. Luo, D. Fu, K. Wu, X. Wang, X. Bian, Z. Lu, X. Chang, Z. Wang, S. Huang, Y. Zhu, J. Zhou, S. Chen, C. Pei, Z. J. Zhao and J. Gong, *Science*, 2025, **390**, 900.
20 H. Du, M. Wang, P. Li, H. Zhao, G. Ma, R. Dong, H. Hou, S. Hu and H. Wang, *Surf. Interfaces*, 2024, **53**, 104987.
21 Y. Liu, S. Liu, M. Chen, Y. Bai, Y. Liu, J. Mei and B. Lai, *J. Hazard. Mater.*, 2024, **461**, 132417.
22 W.-J. Lee, S. Bera, C. M. Kim, E.-K. Koh, W.-P. Hong, S.-J. Oh, E. Cho and S.-H. Kwon, *NPG Asia Mater.*, 2020, **12**, 40.
23 H. Frey, A. Beck, X. Huang, J. A. van Bokhoven and M. G. Willinger, *Science*, 2022, **376**, 982–987.
24 M. Xu, M. Peng, H. Tang, W. Zhou, B. Qiao and D. Ma, *J. Am. Chem. Soc.*, 2024, **146**, 2290–2307.
25 P. Li, Q. Zhu, J. Liu, T. Wu, X. Song, Q. Meng, X. Kang, X. Sun and B. Han, *Chem. Sci.*, 2024, **15**, 3233–3239.

© 2026 The Author(s). Published by the Royal Society of Chemistry

Open Access Article. Published on 12 January 2026. Downloaded on 5/6/2026 12:28:05 AM. This article is licensed under a Creative Commons Attribution-NonCommercial 3.0 Unported Licence.

26 X. Xu, L. Su, X. Yu, J. Sun and X. Miao, *Inorg. Chem. Front.*, 2024, **11**, 1381–1393.
27 K. Yeom, J. Jo, H. Shin, H. Ji, S. Moon, J. E. Park, S. Lee, J. Shim, D. H. Mok, M. S. Bootharaju, S. Back, T. Hyeon and Y. E. Sung, *Adv. Funct. Mater.*, 2024, **34**, 2401095.
28 Y. Huang, F. Kong, X. Yu, T. Yang, P. Wu, R. Shen, S. Zhuo, X. Cui and J. Shi, *Adv. Mater.*, 2025, **37**, 2419887.
29 Y. Tan, Y. Wang, A. Li, X. Jiang, Y. Zhang and C. Cheng, *J. Energy Chem.*, 2024, **96**, 568–577.
30 J. Zhao, W. Han, J. Chen, Y. Meng, B. Hao, X. Liu, T. Wang and X. Li, *Small*, 2024, **20**, 2406583.
31 H.-M. Yang, H.-Y. Wang, S. Zhai, J.-T. Ren and Z.-Y. Yuan, *Chem. Eng. J.*, 2024, **489**, 151236.
32 H. Yan, Z. Jiang, B. Deng, Y. Wang and Z. J. Jiang, *Adv. Energy Mater.*, 2023, **13**, 2300152.
33 M. Xing, D. Zhang, D. Liu, C. Song and D. Wang, *J. Colloid Interface Sci.*, 2023, **629**, 451–460.
34 W. Zhang, H. Wang, J. Jiang, Z. Sui, Y. Zhu, D. Chen and X. Zhou, *ACS Catal.*, 2020, **10**, 12932.
35 B. Sun, H. Lv, Q. Xu, P. Tong, P. Qiao, H. Tian and H. Xia, *Small*, 2024, **20**, 2400240.
36 D. Xue, Y. Yuan, Y. Yu, S. Xu, Y. Wei, J. Zhang, H. Guo, M. Shao and J.-N. Zhang, *Nat. Commun.*, 2024, **15**, 5990.
37 M. Zhao, X. Wang, J. Xu, Y. Li, X. Wang, X. Chu, K. Wang, Z. Wang, L. l. Zhang, J. Feng, S. Song and H. Zhang, *Adv. Mater.*, 2024, **36**, 2313596.
38 J. Yang, S. Song, Z. Chen, B. Zhang, Y. Guo, Y. Guo and H. Zhang, *J. Mater. Chem. A*, 2025, **13**, 6020–6026.
39 H. K. Basak, M. K. Adak, A. Rajput and B. Chakraborty, *ACS Appl. Mater. Interfaces*, 2025, **17**, 9391–9406.
40 L. Vazhayal, S. B. Alex and S. K. Haram, *J. Mater. Chem. A*, 2024, **12**, 27671–27685.
41 T. Jiang, X. Jiang, C. Jiang, J. Wang, Y. Danlos, T. Liu, C. Deng, C. Chen, H. Liao and V. Kyriakou, *Adv. Energy Mater.*, 2025, **15**, 2501634.
42 L. Liu, C. Liu, M. Wang, B. Li, K. Wang, X. Fan, N. Li, H. Wang, S. Hu and X. Diao, *Chem. Eng. J.*, 2023, **456**, 141022.
43 Q. Zhou, C. Xu, J. Hou, W. Ma, T. Jian, S. Yan and H. Liu, *Nano-Micro Lett.*, 2023, **15**, 95.
44 R. S. Mane, H. M. Wilson, B. N. Patil, S. J. Lee and N. Jha, *J. Mater. Chem. A*, 2025, **13**, 36550–36563.
45 N. Bhuvanendran, C. W. Park, H. Su and S. Y. Lee, *Environ. Res.*, 2023, **229**, 115950.
46 Y. Liu, S. Liu, P. Zhang, J. Zhou, H. Liu, S. Li, X. Li, X. Wang, D. Han, Y. Chen, Y. Wang, J. Jiang and B. Li, *Adv. Funct. Mater.*, 2024, **34**, 2400522.
47 Y. Liu, L. Zhang, Q. Xu, S. Zhang, Y. Zhou and G. Hu, *Adv. Funct. Mater.*, 2024, **35**, 2413134.
48 P. Wang, D. Deng, S. Wu and L. Xu, *Chin. J. Struct. Chem.*, 2024, **43**, 100199.
49 Z. He, N. Xu, Y. Wang, D. Chao, R. Maric, A. Virkar and X.-D. Zhou, *Chem. Eng. J.*, 2026, **527**, 171444.
50 S. Qin, K. Li, M. Cao, W. Liu, Z. Huang, G. He, I. P. Parkin and H. Li, *Nano Res. Energy*, 2024, **3**, e9120122.
51 K. S. Smith, C. Adjah-Tetteh, Z. He, G. Yang, Y. Wang, S. Bliznakov, R. Maric, N. Xu and X.-D. Zhou, *J. Phys. Chem. C*, 2025, **129**, 16507–16515.
52 L. Luo, R. Tang, L. Su, J. Kou, X. Guo, Y. Li, X. Cao, J. Cui and S. Gong, *Energy Storage Mater.*, 2024, **72**, 103773.
53 M. Zhang, T. Zhou, D. Bukhvalov, F. Han, C. Wang and X. Yang, *Appl. Catal., B*, 2023, **337**, 122976.
54 B. Li, J. Liu, C. Zhao, A. Hu, X. Sun, B. Mei and J. Long, *Inorg. Chem.*, 2024, **63**, 19322–19331.
55 Y. Xu, W. Zhao, R. Chen, H. Li, X. Liu, P. Wu, H. Yu, J. Wang, L. L. Shen, G. R. Zhang and D. Mei, *Adv. Funct. Mater.*, 2025, e12498.
56 T. Jian, W. Ma, C. Xu, H. Liu and J. Wang, *eScience*, 2023, **3**, 100114.
57 T. Li, D. Zhang, Y. Zhang, D. Yang, R. Li, F. Yu, K. Zhong, X. Su, T. Song, L. Jiao, H.-L. Jiang, G.-P. Sheng, J. Xu, H. Li and Z.-Y. Wu, *Energy Environ. Sci.*, 2025, **18**, 4949–4961.
58 Z. Wan, Z. Ma, X. Deng, Y. Wu, J. Li and X. Wang, *Adv. Energy Mater.*, 2025, **15**, 2501630.
59 M. Huo, Y. Liang, W. Liu, X. Zhang, K. Qin, Y. Ma, Z. Xing, J. Chang and G. Zhu, *Adv. Energy Mater.*, 2024, 2405155.
60 Y. Zhai, X. Ren, J. Zhang, T. Gan, N. Yang, B. Wang and S. Liu, *Small*, 2024, **21**, 2407851.

© 2026 The Author(s). Published by the Royal Society of Chemistry